

PhaseT Ξ M: 3D Imaging at 1.6 Å Resolution via Electron Cryo-Tomography with Nonlinear Phase Retrieval

Juhyeok Lee^{1,2*}, Samuel W. Song³, Min Gee Cho²,
Georgios Varnavides^{3,4}, Stephanie M. Ribet², Colin Ophus^{5,6},
Mary C. Scott^{2,3*}, Michael L. Whittaker^{1,7*}

¹Energy Geosciences Division, Lawrence Berkeley National Laboratory, Berkeley, 94720, CA, USA.

²National Center for Electron Microscopy, Molecular Foundry, Lawrence Berkeley National Laboratory, Berkeley, 94720, CA, USA.

³Department of Materials Science and Engineering, University of California Berkeley, Berkeley, 94720, CA, USA.

⁴Miller Institute for Basic Research in Science, University of California Berkeley, Berkeley, 94720, CA, USA.

⁵Department of Materials Science and Engineering, Stanford University, Stanford, 94305, CA, USA.

⁶Precourt Institute for Energy, Stanford University, Stanford, 94305, CA, USA.

⁷Materials Science Division, Lawrence Berkeley National Laboratory, Berkeley, 94720, CA, USA.

*Corresponding author(s). E-mail(s): jhlee0667@lbl.gov;
mary.scott@berkeley.edu; mwhittaker@lbl.gov;

Abstract

Electron cryo-tomography (cryo-ET) enables 3D imaging of complex, radiation-sensitive structures with molecular detail. However, image contrast from the interference of scattered electrons is nonlinear with atomic density and multiple scattering further complicates interpretation. These effects degrade resolution, particularly in conventional reconstruction algorithms, which assume linearity. Particle averaging can reduce such issues but is unsuitable for heterogeneous or dynamic samples ubiquitous in biology, chemistry, and materials sciences. Here,

we develop a phase retrieval-based cryo-ET method, PhaseT Ξ M. We experimentally demonstrate its application to a ~ 7 nm Co_3O_4 nanoparticle on ~ 30 nm carbon substrate, achieving a maximum resolution of 1.6 Å, surpassing conventional limits using standard cryo-TEM equipment. PhaseT Ξ M uses a multislice model for multiple scattering and Bayesian optimization for alignment and computational aberration correction, with a positivity constraint to recover ‘missing wedge’ information. Applied directly to biological particles, it enhances resolution and reduces artifacts, establishing a new standard for routine 3D imaging of complex, radiation-sensitive materials.

Introduction

Transmission electron microscopy (TEM) enables the formation of two-dimensional (2D) structural images from atomic- to micrometer scales, making it a valuable characterization tool for materials of nearly any composition. However, critical structural details such as defects, interfaces, complex architectures, and weak electron signals are hidden by the projection of the three-dimensional (3D) material potential to 2D [1–5]. Electron tomography (ET) addresses this limitation by combining images from multiple angles to reconstruct 3D volumes from 2D projections. This approach reveals 3D features that are inaccessible with 2D imaging alone [1, 6–11], yet are essential for determining material properties.

Recent advances in ET have pushed its resolution to the atomic scale through the use of aberration-corrected annular dark-field (ADF) scanning transmission electron microscopy (STEM) [1, 5, 7, 10, 12–17]. Despite the advances, ADF-STEM suffers from inherent limitations, including nonlinear contrast due to multiple scattering, a restricted depth of focus, poor sensitivity to light elements, and high electron dose requirements due to slow scanning time. These drawbacks make it less effective for 3D imaging of thick or radiation-sensitive materials [18–24].

In contrast to scanning techniques, conventional TEM (CTEM) uses a parallel electron beam, allowing for rapid, low-dose imaging of dynamic processes and radiation-sensitive materials [8, 11]. CTEM image contrast arises from the interference of scattered electrons from the electrostatic potential. Similar to STEM, stronger electron-atom interactions and increased sample thickness result in more multiple scattering, leading to more nonlinear interference contrast compared to atomic density. Moreover, multiple scattering in samples thicker than approximately twice the mean free electron path [25] degrades beam coherence, and therefore limits resolution. Additional contrast modulation is created by lenses in the imaging system. These effects hinder accurate structural reconstruction using conventional tomography techniques that assume linear contrast [8, 11, 23, 24], except in special cases [26, 27] where electrons scatter only once from a single atom type.

In organic materials, weak electron-atom interactions allow their structures to be determined from single-scattering reconstructions [8, 11], but their radiation sensitivity prevents atomic details from being resolved in individual particles, and their image contrast is not strictly linear. Advanced 3D imaging techniques, such as single-particle

cryo-electron microscopy (cryo-EM), reconstruct the average 3D atomic positions of particles as small as protons with near-atomic resolution [28–33], overcoming radiation sensitivity limits. However, these techniques are limited to materials with thousands of nearly identical copies that can be averaged together, which precludes their application to heterogeneous materials.

Interpretable 3D imaging of arbitrary materials requires a physical model to solve the electron-atom scattering problem and instrumental contrast transfer modulation to overcome their limitations, while also being robust to noise arising from sensitive or thick samples. Emerging 3D phase retrieval algorithms based on the multislice method address these limitations by solving the inverse scattering problems and enabling reliable 3D reconstruction of thick samples under low electron doses [23, 24, 34–38]. STEM-based 3D phase retrieval has recently made major advances in retrieving 3D phase information with improved resolution and sensitivity to light elements. [39–42]. However, implementing these methods broadly in practice remains challenging, especially for radiation-sensitive materials, due to beam damage from the intense probe, long acquisition times for large areas, and distortions from scan instabilities. In contrast, high-resolution TEM (HRTEM) in CTEM enables fast imaging over large fields of view. Combined with fractional imaging and motion correction, it can achieve high resolution without significant loss, even for radiation-sensitive materials [43–45].

Here, we experimentally demonstrate an HRTEM tomography method based on phase retrieval, PhaseTEM, showing that 3D phase-contrast imaging can achieve a maximum resolution of 1.6 Å on a standard cryo-electron microscope without physical aberration correction. We reconstructed a 7 nm Co_3O_4 nanoparticle supported on 30 nm of carbon using the multislice model to account for multiple scattering and Bayesian optimization to computationally correct image and tilt alignment, contrast transfer, and microscope aberrations. Using the same method, we also reconstructed HIV-1 (human immunodeficiency virus) particles from the publicly available EMPIAR-10164 dataset [30], achieving a resolution of 9.0 nm, which represents approximately 20-30% improvement compared to conventional reconstruction methods. Our method is applicable to both organic and inorganic materials, vitrified in ice or under vacuum. Autonomous data acquisition and reconstruction scripts are widely available and easily implemented on standard commercial microscopes, making this a powerful scientific tool that spans materials, biological, physical, chemical, and geological sciences.

Results

Tomography Experiment Setup

Figure 1a-c shows the experiment setup of our 3D phase-contrast tomography, PhaseTEM. We collected a tomographic tilt series of Co_3O_4 nanoparticles supported by a carbon grid, by acquiring HRTEM images at tilt angles ranging from -65° to $+65^\circ$ in 1° increments. At each tilt angle, three images were acquired at different defocus values. The electron dose per image was $21.5 e^-/\text{Å}^2$, resulting in a total accumulated dose of $8,460 e^-/\text{Å}^2$ across the entire series. As shown in Fig. 1d-f, we

performed image preprocessing for 3D reconstruction. These steps include motion correction, focal and tilt alignment, estimation of microscopy parameters, and denoising (see Methods). From the preprocessed tilt series, we reconstructed a 3D potential of the sample, which includes an approximately 7 nm diameter Co_3O_4 nanoparticle and a 30 nm thick amorphous carbon support. To retrieve 3D phase structural information and account for multiple scattering, we applied a forward and inverse multislice approach [36, 46] (see Methods), as illustrated in Fig. 1g. We iteratively refined the 3D reconstructed potential using the gradient descent method, minimizing the differences between the calculated projections from the estimated 3D potential and the experimentally measured projections.

Experimental Tomography via Phase Retrieval

The reconstructed volume in Fig. 2a represents a 3D potential of the 7 nm Co_3O_4 nanoparticle partially embedded in the 30 nm carbon support. The intensity of the reconstructed potential is approximately proportional to the atomic number: lighter elements like carbon and oxygen appear with lower intensity, while heavier elements like cobalt show higher intensity. As seen in Fig. 2a, the Co_3O_4 nanoparticle and the carbon support are clearly distinguishable.

To estimate the quality and resolution of the 3D reconstruction, we reconstructed a 3D potential using a cropped tilt series focusing on the Co_3O_4 nanoparticle with a pixel size of 0.52 Å (see Methods). We then applied a 3D mask to the reconstructed volume in Fig. 2b to remove the intensity of the carbon support film. As shown in Fig. 2c, the central slices of the 3D reconstructed volume along different axes reveal bright atomic intensities and lattice lines of the nanoparticle. The 2D Fourier transform of each central slice shows the {400} diffraction peak at a resolution of 2 Å, except for the slice where the missing wedge region overlaps with one of the {400} diffraction peaks. The 3D Fourier transform of the 3D reconstructed image in Fig. 2d also exhibits diffraction peaks at 2 Å resolution, consistent with the 2D Fourier transform results. Figure 2e shows a 3D isosurface image with a lower threshold than that in Fig. 2d, presented from a different viewpoint to highlight the missing wedge region. Interestingly, the diffraction peaks of 4.6 Å {111} and 2.8 Å {220} resolution in the missing wedge region were restored. This improvement is attributed to the application of a physical constraint, positivity (i.e., enforcing nonnegative potential values), which helps suppress missing wedge artifacts and the elongation effect, ultimately aiding in the recovery of diffraction peaks. As shown in Supplementary Fig. 1, only the reconstruction with the positivity constraint exhibits the recovery of diffraction peaks within the missing wedge. Additionally, {422} diffraction peaks at 1.6 Å resolution in Fig. 2d-e are visible, indicating the high-resolution capability of our reconstruction. This suggests that the maximum resolution of our 3D reconstruction is 1.6 Å. However, due to the limited tilt range and single, fixed rotation axis, the resolution is anisotropic, varying depending on direction. We also plotted the power spectrum in Fig. 2f to cross-check the resolution estimation, and the results are consistent with the previous Fourier transform analysis. Lastly, to investigate the effect of multiple scattering correction using the inverse multislice method, we compared slices from volumes reconstructed with the multislice and single-slice phase retrieval approaches. As

seen in [Supplementary Fig. 2](#), multiple scattering correction via the multislice method improves the resolution.

Simulated Tomography via Phase Retrieval

To verify the resolution estimated from our experimental reconstruction, we conducted simulations to reproduce our phase retrieval-based tomography experiment. By comparing the experimental and simulated results, we confirmed the validity of our resolution estimation. As shown in [Fig. 3a](#), we first created 3D atomic positions of a Co_3O_4 nanoparticle and an amorphous carbon membrane (see Methods). Next, we performed TEM simulations to generate the simulated tilt and focal series under the same experimental conditions. We applied Poisson noise to match the electron dose level used in the experiment (see Methods). Finally, we reconstructed a 3D potential from the simulated tilt series using the same reconstruction process as in the experiment (see Methods). We then applied a 3D mask to the reconstructed volume to extract the nanoparticle intensity.

Following the same resolution analysis as performed on the experimental results, we evaluated the simulated reconstruction. [Figure 3b](#) shows the 3D density map of the reconstructed volume of the Co_3O_4 nanoparticle. The central slice of the 3D volume in [Fig. 3c](#) exhibits bright atomic intensities with clear lattice fringes. As seen in [Fig. 3c](#), the $\{400\}$ diffraction peaks at a resolution of 2 Å are visible in all the Fourier transform images. In comparison, these $\{400\}$ diffraction peaks are absent in the missing wedge region of the experimental results ([Fig. 2c](#)) at the same resolution. This difference is due to imperfections in alignment, parameter estimation, and noise modeling, as well as limitations of the tomography method, which cannot fully account for all experimental effects, such as inelastic scattering. It is well known that simulation results generally outperform experimental ones because they do not consider all sources of systematic errors and artifacts present in experimental data [47]. The 3D isosurface plots of the 3D Fourier transform images in [Fig. 3d-e](#) exhibit diffraction peaks at 1.6 Å resolution, similar to the experiment results. A different 3D view in [Fig. 3e](#), highlighting the missing wedge region, also shows retrieved diffraction peaks and faint peaks at 1.4 Å resolution. These results are consistent with the power spectrum in [Fig. 3f](#). The simulated 3D reconstruction, which mimics our experimental conditions, demonstrates results comparable to the experimental data in terms of resolution and diffraction peak retrieval within the missing wedge region.

Comparative analysis of phase retrieval and conventional tomography

To compare our approach with conventional tomography, we reconstructed the 3D volume of the Co_3O_4 nanoparticle and its carbon support using the projection-based tomography algorithm, specifically the simultaneous iterative reconstruction technique (SIRT) (see Methods) [48]. As shown in [Fig. 4a,e](#) and [Supplementary Fig. 2a,d](#), both the multislice and single-slice phase retrieval methods can retrieve not only the nanoparticle but also the carbon support, whereas conventional tomography fails to reconstruct the carbon support. This suggests that the ability to solve the inverse

scattering problem is the critical factor for reconstructing the carbon support, rather than multiple scattering correction. In [Supplementary Fig. 3c-d](#), the carbon intensity is even lower than the vacuum area, and ring-shaped artifacts appear prominently at the boundaries due to nonlinear complex interference contrast, which violates the tomography projection rule.

To further evaluate the performance of the two tomography methods, we compared cropped regions close to the nanoparticle. As shown in [Fig. 4b,f](#), both methods enable the reconstruction of the nanoparticle structures. However, phase retrieval provides higher overall quality and resolution than conventional tomography. This is supported by the Fourier images in [Fig. 4d,h](#) and [Supplementary Fig. 4c,f](#), which show higher index diffraction peaks for phase-contrast imaging. Specifically, [Figure 2](#) demonstrates a resolution of 1.6–2.0 Å for phase retrieval imaging, whereas [Supplementary Figure 5c-f](#) shows a SIRT reconstruction resolution of 2.0–2.4 Å, similar to the diffraction limit ([Supplementary Fig. 6](#)). Additionally, the brighter intensities observed at the nanoparticle boundaries in [Fig. 4g](#) and [Supplementary Fig. 4e](#) indicate a deficiency in low-frequency information in the SIRT reconstruction. In contrast, the phase retrieval-based reconstruction compensates for these anisotropic intensities by effectively retrieving the missing frequency information through the lens transfer characteristics. This capability can be demonstrated by simulations of the spectral signal-to-noise ratio (SSNR) in 2D focal series reconstruction, presented in [Supplementary Fig. 7](#). The SSNR indicates that information can be retrieved even at the zero-crossing points of the CTF in raw HRTEM images, where contrast transfer is otherwise absent (see Methods).

HIV-1 particles reconstruction

A major advantage of our method is that it can be directly applied to typical HRTEM tomographic tilt data, including open-source datasets such as EMPIAR. Notably, while the previous example used tomographic tilt data acquired with multiple defocus values, our method is also applicable to tilt series collected at a single defocus, enabling the retrieval of the full 3D phase volume.

To demonstrate the flexibility of our 3D method, we applied it to a biological sample, HIV-1 particles, using the publicly available EMPIAR-10164 dataset [30]. We reconstructed the 3D volume of HIV-1 particles using the phase retrieval and conventional tomography methods for comparison. [Figure 5](#) presents the 3D volumes obtained from our phase retrieval method and the SIRT algorithm [48], clearly showing the ring-shaped structures of HIV-1 particles and bright fiducial gold markers. First, as shown in [Fig. 5c](#), the FSC resolution achieved by our method is 9.0 nm, surpassing the 13.1 nm resolution obtained with SIRT reconstruction (see Methods). Furthermore, as presented in [Supplementary Fig. 8](#), we compared our method with various other reconstruction techniques, demonstrating superior correlation results. It is important to note that these results are based on a single tilt series, leading to a significantly lower resolution than the previously reported value obtained using sub-tomogram averaging [30]. Furthermore, as observed with the Co_3O_4 nanoparticle reconstructions ([Fig. 4e](#)), the SIRT reconstruction ([Fig. 5b](#)) exhibits noticeable ring-shaped artifacts near the edges because the interference contrast does not strictly satisfy the assumptions of the

tomographic projection theorem. In contrast, our method effectively mitigates these artifacts, underscoring its robustness in addressing multiple scattering phenomena. Lastly, the enlarged images of HIV-1 particles reconstructed with our phase retrieval method (Fig. 5d-e) exhibit sharper structural features compared to those obtained with the SIRT algorithm (Fig. 5f-g).

It is worth noting that organic materials, such as HIV-1, are composed of light elements and generally exhibit weak electron-atom scattering. This is supported by the observation that the multislice and single-slice FSC curves are nearly identical, with the multislice result showing a very slight improvement, as shown in [Supplementary Fig. 8](#). Consequently, conventional reconstruction methods, including computationally efficient, non-iterative approaches such as back projection-based methods, can yield reasonably accurate results for such samples, particularly when combined with particle averaging techniques. However, the objective of this work is to demonstrate that our physics-based phase retrieval framework can be directly applied to biological datasets and still provide improved resolution and artifact suppression, even from a single tomographic tilt series. Importantly, we anticipate that the benefits of our method will be more pronounced for thicker or more structurally heterogeneous biological specimens, where multiple scattering and interference effects degrade the performance of conventional reconstruction algorithms.

Discussion

In this study, we present PhaseT_{EM}, a 3D phase retrieval-based tomography for high-resolution imaging using multiple tilted HRTEM focal series. By advancing phase retrieval techniques and developing algorithms for sub-pixel alignment and precise parameter optimization, we successfully reconstructed an approximately 7 nm Co₃O₄ nanoparticle embedded in an approximately 30 nm thick carbon support. This marks the first demonstration of near-atomic resolution 3D phase contrast imaging from a single HRTEM tilt and focal series, overcoming major challenges such as nonlinear artifacts.

Our method introduces several key innovations that contribute to the improved reconstruction: (1) an inverse model that enables accurate 3D potential reconstruction, including weakly scattering components such as the carbon support; (2) a multislice formulation that corrects for nonlinear effects arising from multiple scattering, thereby improving resolution; and (3) a positivity constraint that helps recover missing wedge information, enhancing Fourier completeness and reducing reconstruction artifacts.

Beyond nanoparticle systems, PhaseT_{EM} is broadly applicable to open-source datasets, including biological samples, without the need for specialized hardware. This is particularly valuable for biological imaging, where structural complexity and low-dose requirements are critical. The method is also compatible with single-particle techniques in cryo-EM and cryo-ET, enabling detailed 3D structural analysis of radiation-sensitive materials.

Although PhaseT_{EM} avoids restrictive approximations and significantly improves accuracy, it currently requires substantial computational resources, approximately 100

times more than conventional methods. However, as GPU technology and computational tools continue to improve, we expect this approach to become increasingly practical and accessible. In the near future, the ability to extract high-fidelity 3D structural information without simplifying assumptions represents a major step forward, paving the way for new discoveries across materials science, biology, and beyond.

Figures

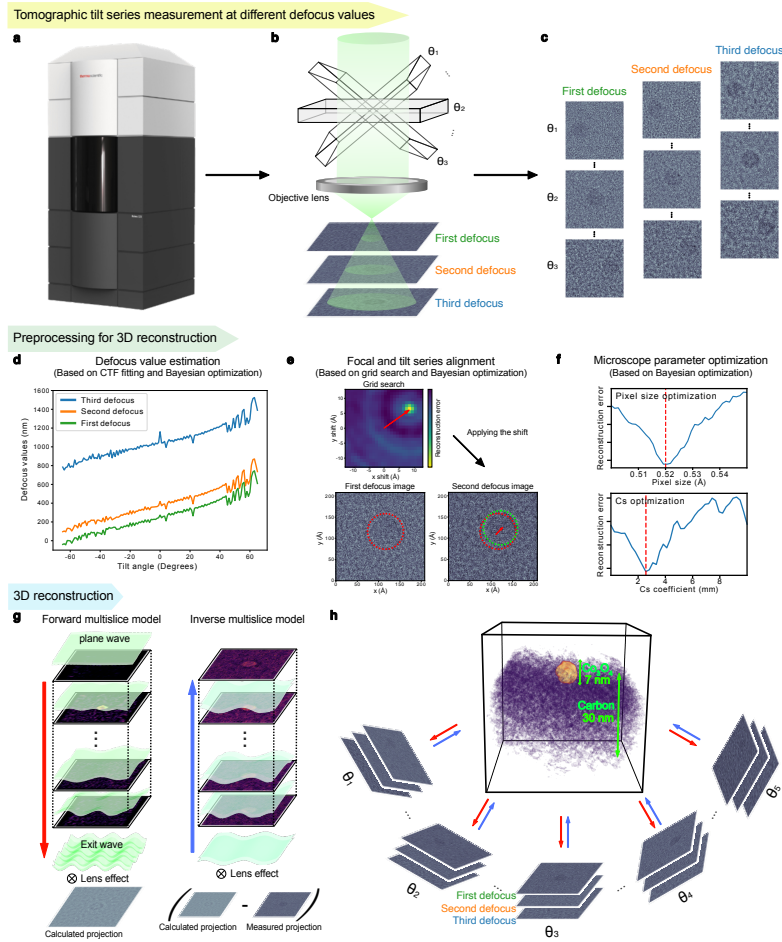


Fig. 1 Steps for Experimental Phase Retrieval-based Electron Cryo-Tomography, PhaseTEM. **a-c**, Workflow for collecting tomographic tilt-series data at multiple defocus values. **a**, Photograph of a commercial Cryo-TEM setup for measuring HRTEM tomographic data. **b**, Schematic illustration of tomographic tilt-series acquisition at different defocus levels. **c**, Acquisition of HRTEM tilt series images at multiple defocus settings using a standard Cryo-TEM instrument. **d-f**, Preprocessing steps for 3D reconstruction. **d**, Plot illustrating the estimated defocus values at each tilt angle, showing tilt-dependent variations. **e**, Alignment procedure, where the optimal alignment with minimal reconstruction error is identified through a grid search for 2D shifts. **f**, Estimation of microscope parameters via Bayesian optimization to minimize reconstruction errors. **g-h**, Workflow for experimental tomography reconstruction. **g**, Forward and inverse multislice models for solving the scattering problem. At each tilt angle, the multislice forward model calculates simulated HRTEM projections, and the inverse model reconstructs the 3D volume. **h**, Schematic illustration of phase contrast tomography setup. The phase contrast tomography directly reconstructs the 3D potential using multiple tilted focal series of HRTEM images. The 3D volume within the black box represents the reconstructed potential of a Co_3O_4 nanoparticle embedded in a thick carbon support. Note that, to enhance visualization, distinct color scales are applied to differentiate the Co_3O_4 nanoparticle from the carbon support. The total 3D reconstruction achieves a voxel size of 2.08 Å, after applying a binning factor of 4.

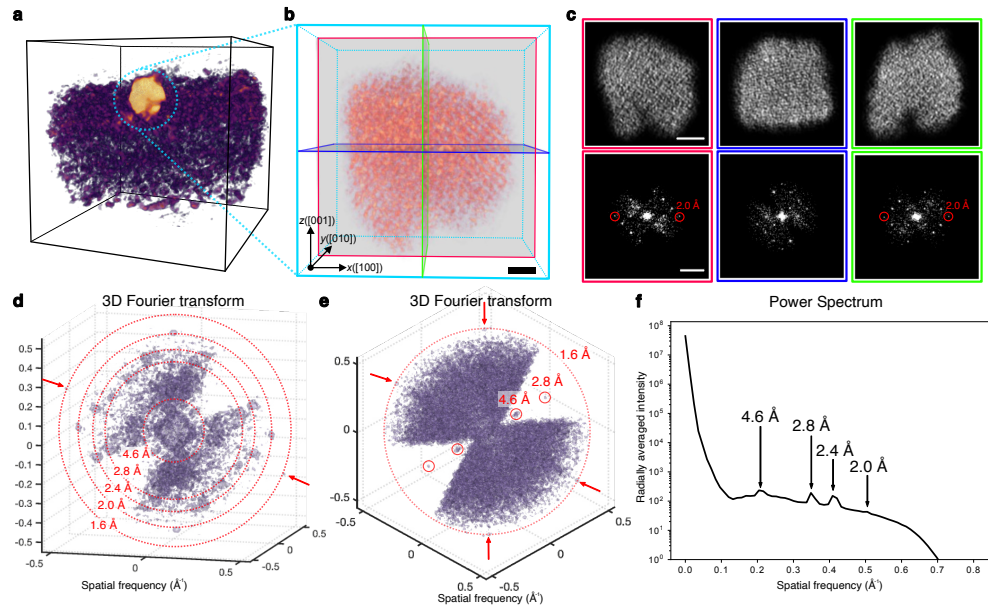


Fig. 2 Experimental 3D Reconstruction with Phase Retrieval (PhaseTEM) and Resolution Analysis. **a**, Half-sectioned 3D density map showing the internal cross-section of the full 3D reconstruction of a Co_3O_4 nanoparticle partially embedded in a carbon support. **b**, 3D density map of the Co_3O_4 nanoparticle after applying a 3D mask to remove the carbon support. Scale bar: 1 nm. **c**, Top panel: 2-Å thick central slices of the 3D reconstruction in (b), with frame colors corresponding to the slice positions in the 3D volume of (b). Bottom panel: 2D Fourier transform of the central slice shown in the top panel. Scale bars: Top panel, 2 nm; Bottom panel, 0.4 \AA^{-1} . **d**, 3D Fourier transform of the reconstruction in (b), displaying diffraction peaks at up to 1.6 \AA resolution. **e**, 3D Fourier transform of the reconstruction in (b) from a different view, highlighting the missing wedge region. The image shows restored diffraction peaks within the missing wedge and weak diffraction peaks at 1.6 \AA resolution. Red arrows indicate the 1.6 \AA resolution peaks. **f**, Power spectrum of the 3D reconstruction shown in (b), indicating a resolution limit of 2.0 \AA .

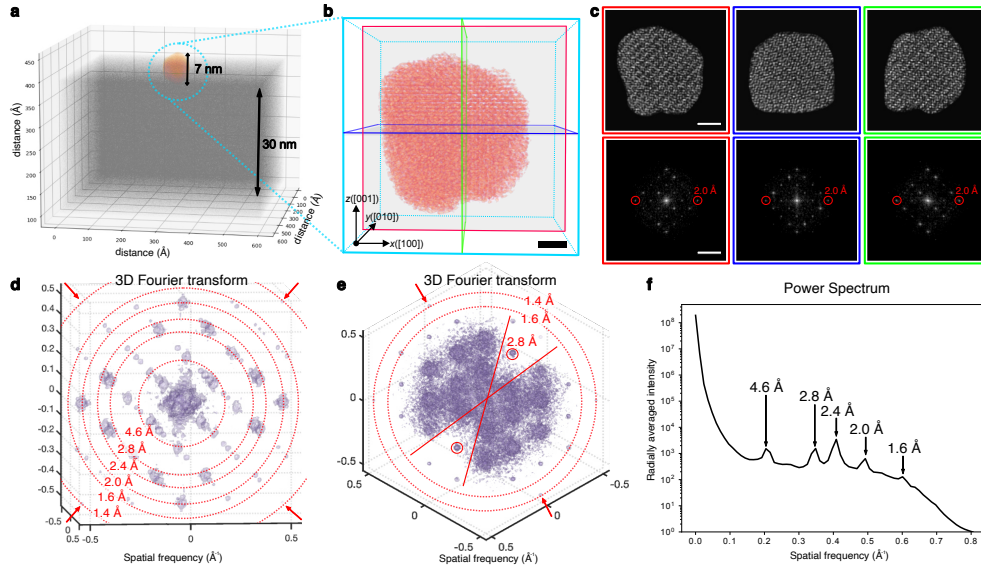


Fig. 3 Simulated 3D Reconstruction with Phase Retrieval (PhaseT3M) and Resolution Analysis. **a**, 3D atomic models of the Co_3O_4 nanoparticle and the carbon support. The 3D atomic position of the Co_3O_4 nanoparticle is based on a perfect crystal, whereas the 3D atomic position of the amorphous carbon support is generated randomly. **b**, 3D density map of the Co_3O_4 nanoparticle after applying a 3D mask to remove the carbon support. Scale bar: 1 nm. **c**, Top panel: 2-Å thick central slices of the 3D reconstruction in (b), with each color frame corresponding to the slice color in the 3D reconstruction. Bottom panel: 2D Fourier transform of the central slice shown in the top panel. Scale bars: Top panel, 2 nm; Bottom panel, 0.4 \AA^{-1} . **d**, 3D Fourier transform of the reconstruction in (b), displaying diffraction peaks at 1.4 Å resolution. **e**, 3D Fourier transform of the reconstruction in (b) from a different view, highlighting the missing wedge region. The image reveals restored diffraction peaks within the missing wedge and weak diffraction peaks at 1.4 Å resolution. The red arrows represent the 1.4 Å resolution limit. **f**, Power spectrum of the 3D reconstruction in (b), indicating a resolution of 1.6 Å.

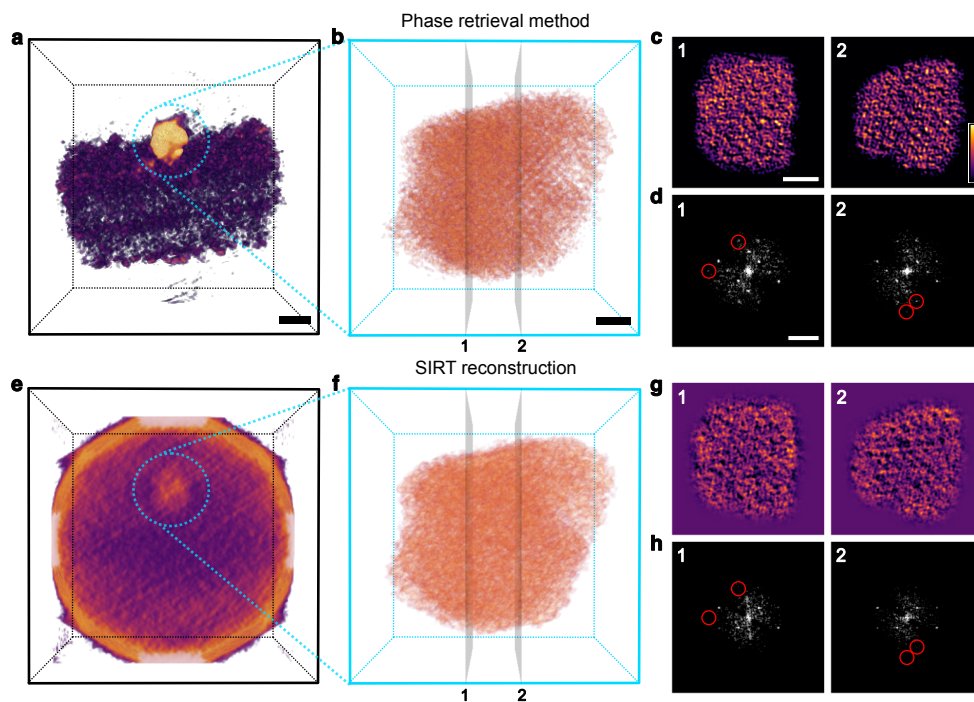


Fig. 4 Comparative Analysis of Phase Retrieval (PhaseTEM) and SIRT Reconstructions for the Co_3O_4 nanoparticle. **a, e,** 3D density maps of the Co_3O_4 nanoparticle and the carbon support reconstructed using phase retrieval (PhaseTEM) (a) and SIRT (e). The 3D volumes were reconstructed with a voxel size of 2.08 Å. Scale bar: 5 nm. **b, f,** 3D density maps of the Co_3O_4 nanoparticle reconstructed using phase retrieval (PhaseTEM) (b) and SIRT (f), after applying a 3D mask to remove the carbon support intensity. The 3D volumes were reconstructed with a voxel size of 0.52 Å. Scale bar: 1 nm. **c, g,** 1 Å-thick slices extracted from the 3D reconstructions in (b) and (f), respectively. Scale bar: 2 nm. **d, h,** 2D Fourier transforms of the slices shown in (c) and (g), respectively. Red circles indicate diffraction peaks present in (d) but absent in (h). Scale bar: 0.4 \AA^{-1} . The slice numbers in (c–d) and (g–h) correspond to the slice positions indicated in the 3D reconstructions in (b) and (f), respectively.

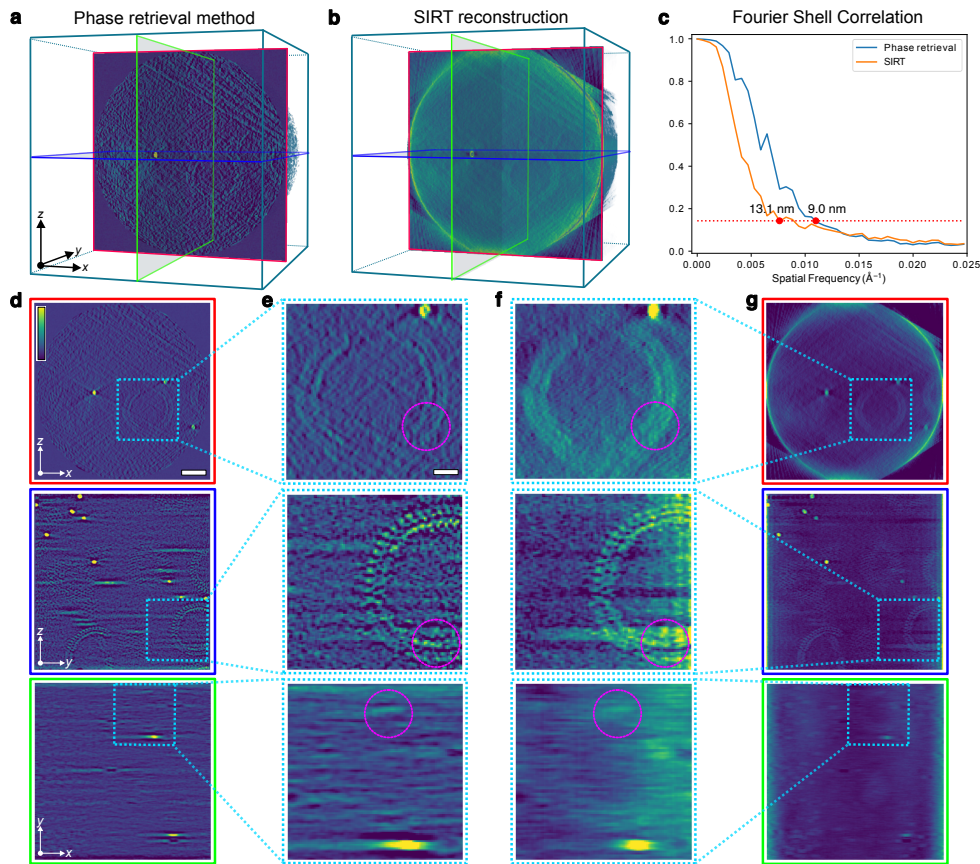


Fig. 5 Comparative Analysis of Phase Retrieval (PhaseTEM) and SIRT Reconstructions of HIV-1 Particles (EMPIAR-10164). **a-b,** Half-sectioned 3D density maps showing the internal cross-sections of the full 3D reconstructions of HIV-1 particles using our phase retrieval method (PhaseTEM) (a) and the SIRT algorithm (without positivity) (b). Faint, ring-shaped features correspond to HIV-1 particles, while bright, spherical intensities represent gold fiducial markers. **c,** Fourier shell correlation (FSC) plots comparing the resolution of 3D reconstructions obtained from our phase retrieval method (a) and the SIRT algorithm (b). The FSC resolutions, determined using the 0.143 criterion, are 9.0 nm for phase contrast tomography and 13.1 nm for SIRT, respectively. **d, e,** 24 nm-thick slices extracted from the reconstructions using our phase-contrast tomography (d) and the SIRT (e), corresponding to the 3D volumes shown in (a) and (b), respectively. The frame colors indicate their positions within the 3D volumes shown in (a) and (b). Scale bars: 50 nm. **e, f,** Enlarged views (3×) of the boxed regions in the phase retrieval slice (d) and the SIRT reconstruction slice (e), respectively. Pink dotted rings highlight regions where our phase-retrieval-based tomography shows improved resolution compared to the SIRT reconstruction. Scale bars: 150 nm.

Acknowledgements. The work of J.L. and M.L.W. was supported by the U.S. Department of Energy, Office of Science, Office of Basic Energy Sciences, Early Career Research Program and Geosciences programs under Award No. DE-AC02-05-CH11231. S.W.S. is supported by the National Science Foundation Graduate Research Fellowship Program under Grant No. DGE 2146752. Any opinions, findings, conclusions or recommendations expressed in this material are those of the authors and do not necessarily reflect the views of the National Science Foundation.

This work was carried out using shared experimental facilities at the California Institute for Quantitative Biosciences at the University of California, Berkeley. We thank Dr. Dan Toso and Dr. Ravi Thakkar for their support with acquiring the experimental cryo-ET data.

Declarations

- Data availability
All of our experimental tilt data and tomographic reconstructions will be posted on a public website upon publication.
- Code availability
The PhaseT \exists M source code is available at the GitHub repository:
(<https://github.com/PhaseT3M/PhaseT3M>).

References

- [1] Van Aert, S., Batenburg, K. J., Rossell, M. D., Erni, R. & Van Tendeloo, G. Three-dimensional atomic imaging of crystalline nanoparticles. *Nature* **470**, 374–377 (2011).
- [2] Chen, C.-C. *et al.* Three-dimensional imaging of dislocations in a nanoparticle at atomic resolution. *Nature* **496**, 74–77 (2013).
- [3] Renaud, J.-P. *et al.* Cryo-em in drug discovery: achievements, limitations and prospects. *Nature Reviews Drug Discovery* **17**, 471–492 (2018).
- [4] Turk, M. & Baumeister, W. The promise and the challenges of cryo-electron tomography. *FEBS Letters* **594**, 3243–3261 (2020).
- [5] Lee, J., Jeong, C., Lee, T., Ryu, S. & Yang, Y. Direct observation of three-dimensional atomic structure of twinned metallic nanoparticles and their catalytic properties. *Nano Letters* **22**, 665–672 (2022).
- [6] Midgley, P. A. & Dunin-Borkowski, R. E. Electron tomography and holography in materials science. *Nature Materials* **8**, 271–280 (2009).
- [7] Scott, M. C. *et al.* Electron tomography at 2.4-ångström resolution. *Nature* **483**, 444–447 (2012).
- [8] Maaz, K. *The Transmission Electron Microscope: Theory and Applications* (BoD – Books on Demand, 2015).
- [9] Ercius, P., Alaidi, O., Rames, M. J. & Ren, G. Electron tomography: A three-dimensional analytic tool for hard and soft materials research. *Advanced Materials* **27**, 5638–5663 (2015).
- [10] Zhou, J., Yang, Y., Ercius, P. & Miao, J. Atomic electron tomography in three and four dimensions. *MRS Bulletin* **45**, 290–297 (2020).
- [11] Ilett, M. *et al.* Analysis of complex, beam-sensitive materials by transmission electron microscopy and associated techniques. *Philosophical Transactions of the Royal Society A: Mathematical, Physical and Engineering Sciences* **378**, 20190601 (2020).
- [12] Rose, H. Correction of aberrations, a promising means for improving the spatial and energy resolution of energy-filtering electron microscopes. *Ultramicroscopy* **56**, 11–25 (1994).
- [13] Rose, H. H. Historical aspects of aberration correction. *Journal of Electron Microscopy* **58**, 77–85 (2009).
- [14] Hetherington, C. Aberration correction for tem. *Materials Today* **7**, 50–55 (2004).

- [15] Goris, B. *et al.* Three-dimensional elemental mapping at the atomic scale in bimetallic nanocrystals. *Nano Letters* **13**, 4236–4241 (2013).
- [16] Yang, Y. *et al.* Deciphering chemical order/disorder and material properties at the single-atom level. *Nature* **542**, 75–79 (2017).
- [17] Lee, J., Jeong, C. & Yang, Y. Single-atom level determination of 3-dimensional surface atomic structure via neural network-assisted atomic electron tomography. *Nature Communications* **12**, 1962 (2021).
- [18] Treacy, M. M. J. & Gibson, J. M. Coherence and multiple scattering in “z-contrast” images. *Ultramicroscopy* **52**, 31–53 (1993).
- [19] Hartel, P., Rose, H. & Dinges, C. Conditions and reasons for incoherent imaging in stem. *Ultramicroscopy* **63**, 93–114 (1996).
- [20] Midgley, P. A. & Weyland, M. 3d electron microscopy in the physical sciences: the development of z-contrast and efem tomography. *Ultramicroscopy* **96**, 413–431 (2003).
- [21] Xin, H. L. & Muller, D. A. Aberration-corrected adf-stem depth sectioning and prospects for reliable 3d imaging in s/tem. *Journal of Electron Microscopy* **58**, 157–165 (2009).
- [22] Krivanek, O. L. *et al.* Atom-by-atom structural and chemical analysis by annular dark-field electron microscopy. *Nature* **464**, 571–574 (2010).
- [23] Kirkland, E. J. *Advanced Computing in Electron Microscopy* (Springer International Publishing, Cham, 2020). URL <http://link.springer.com/10.1007/978-3-030-33260-0>.
- [24] Lee, J., Lee, M., Park, Y., Ophus, C. & Yang, Y. Multislice electron tomography using four-dimensional scanning transmission electron microscopy. *Physical Review Applied* **19**, 054062 (2023).
- [25] Martynowycz, M. W., Clabbers, M. T. B., Unge, J., Hattne, J. & Gonen, T. Benchmarking the ideal sample thickness in cryo-em. *Proceedings of the National Academy of Sciences* **118**, e2108884118 (2021).
- [26] Park, J. *et al.* 3d structure of individual nanocrystals in solution by electron microscopy. *Science* **349**, 290–295 (2015).
- [27] Kim, B. H. *et al.* Critical differences in 3d atomic structure of individual ligand-protected nanocrystals in solution. *Science* **368**, 60–67 (2020).
- [28] Kühlbrandt, W. The resolution revolution. *Science* **343**, 1443–1444 (2014).

- [29] Cheng, Y. Single-particle cryo-em at crystallographic resolution. *Cell* **161**, 450–457 (2015).
- [30] Schur, F. K. M. *et al.* An atomic model of hiv-1 capsid-sp1 reveals structures regulating assembly and maturation. *Science* **353**, 506–508 (2016).
- [31] Nakane, T. *et al.* Single-particle cryo-em at atomic resolution. *Nature* **587**, 152–156 (2020).
- [32] Yip, K. M., Fischer, N., Paknia, E., Chari, A. & Stark, H. Atomic-resolution protein structure determination by cryo-em. *Nature* **587**, 157–161 (2020).
- [33] Liu, H.-F. *et al.* nextpyp: a comprehensive and scalable platform for characterizing protein variability in situ using single-particle cryo-electron tomography. *Nature Methods* **20**, 1909–1919 (2023).
- [34] Van den Broek, W. & Koch, C. T. Method for retrieval of the three-dimensional object potential by inversion of dynamical electron scattering. *Physical Review Letters* **109**, 245502 (2012).
- [35] Van den Broek, W. & Koch, C. T. General framework for quantitative three-dimensional reconstruction from arbitrary detection geometries in tem. *Physical Review B* **87**, 184108 (2013).
- [36] Ren, D., Ophus, C., Chen, M. & Waller, L. A multiple scattering algorithm for three dimensional phase contrast atomic electron tomography. *Ultramicroscopy* **208**, 112860 (2020).
- [37] Chang, D. J. *et al.* Ptychographic atomic electron tomography: Towards three-dimensional imaging of individual light atoms in materials. *Physical Review B* **102**, 174101 (2020).
- [38] Whittaker, M. L. *et al.* Ion complexation waves emerge at the curved interfaces of layered minerals. *Nature Communications* **13**, 3382 (2022).
- [39] Pelz, P. M. *et al.* Solving complex nanostructures with ptychographic atomic electron tomography. *Nature Communications* **14**, 7906 (2023).
- [40] Romanov, A., Cho, M. G., Scott, M. C. & Pelz, P. Multi-slice electron ptychographic tomography for three-dimensional phase-contrast microscopy beyond the depth of focus limits. *Journal of Physics: Materials* **8**, 015005 (2024).
- [41] You, S., Romanov, A. & Pelz, P. M. Near-isotropic sub-Ångstrom 3d resolution phase contrast imaging achieved by end-to-end ptychographic electron tomography. *Physica Scripta* **100**, 015404 (2024).
- [42] Kim, N. Y. *et al.* Determining 3d atomic coordinates of light-element quantum materials using ptychographic electron tomography (2025). URL <http://arxiv>.

[org/abs/2504.08228](https://arxiv.org/abs/2504.08228). ArXiv:2504.08228 [cond-mat].

- [43] Li, X. *et al.* Electron counting and beam-induced motion correction enable near-atomic-resolution single-particle cryo-em. *Nature Methods* **10**, 584–590 (2013).
- [44] Zheng, S. Q. *et al.* Motioncor2: anisotropic correction of beam-induced motion for improved cryo-electron microscopy. *Nature Methods* **14**, 331–332 (2017).
- [45] Zheng, S. *et al.* Aretomo: An integrated software package for automated marker-free, motion-corrected cryo-electron tomographic alignment and reconstruction. *Journal of Structural Biology: X* **6**, 100068 (2022).
- [46] Ren, D., Whittaker, M., Ophus, C. & Waller, L. Distributed reconstruction algorithm for electron tomography with multiple-scattering samples (2021). URL <http://arxiv.org/abs/2110.07857>. ArXiv:2110.07857.
- [47] Krause, F. F. *et al.* Comparison of intensity and absolute contrast of simulated and experimental high-resolution transmission electron microscopy images for different multislice simulation methods. *Ultramicroscopy* **134**, 94–101 (2013).
- [48] Gilbert, P. Iterative methods for the three-dimensional reconstruction of an object from projections. *Journal of Theoretical Biology* **36**, 105–117 (1972).

Supplementary information

Supplementary Figures

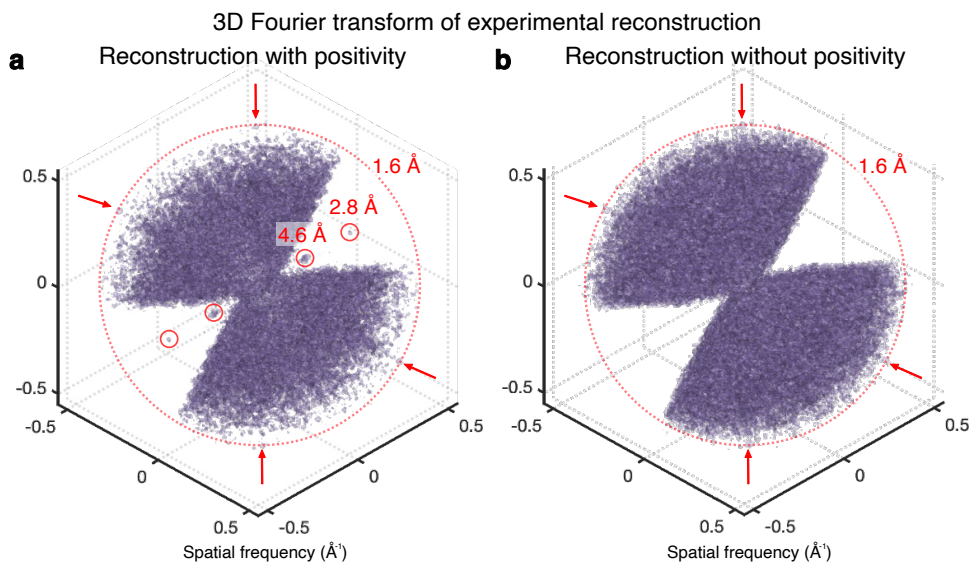


Fig. S1 Comparison of Missing Wedge Recovery with and without Positivity Constraint
a, 3D Fourier transform of the experimental PhaseTEM reconstruction of the Co_3O_4 nanoparticle shown in Fig. 2b, displaying recovered diffraction peaks within the missing wedge due to the positivity constraint. **b**, 3D Fourier transform of the reconstruction without the positivity constraint, showing no recovery of diffraction peaks in the missing wedge.

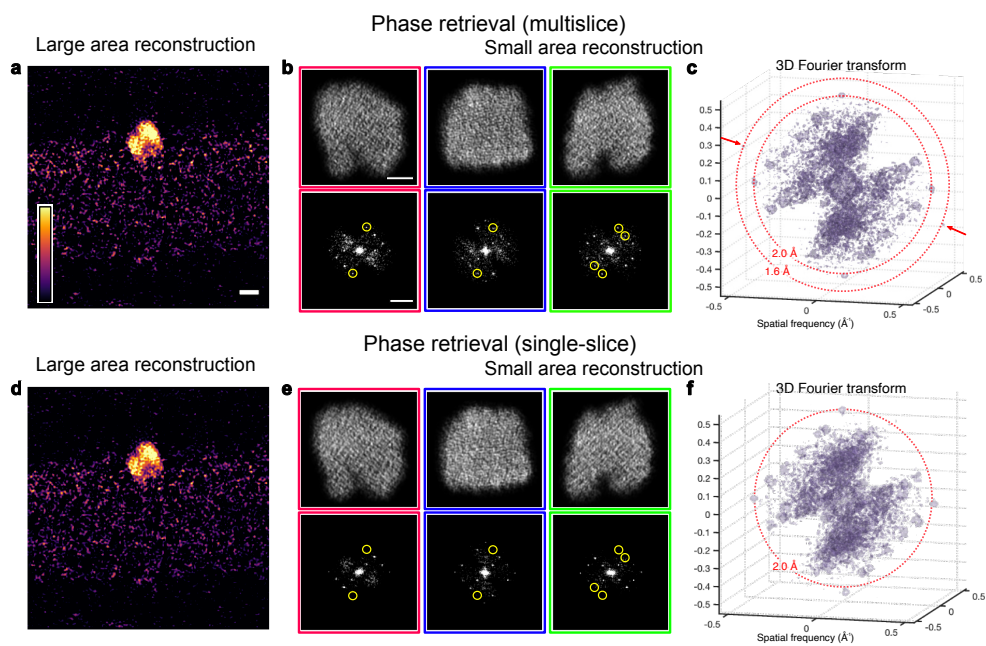


Fig. S2 Comparison of multislice and single-slice PhaseTEM reconstructions. **a, d**, 4 Å-thick near-central 3D slices of the Co_3O_4 nanoparticle and its carbon support, reconstructed using the multislice (**a**) and single-slice (**d**) phase retrieval methods. Scale bar: 4 nm. **b, e**, 2 Å-thick slices extracted from the 3D reconstructions using multislice (**b**) and single-slice (**e**) phase retrieval methods. Slice colors correspond to the slice locations indicated in Fig. 2b–c. Yellow circles highlight diffraction peaks that are present only in the multislice reconstruction and absent in the single-slice result. Scale bar: 1 nm. **c, f**, 3D Fourier transforms of the reconstructions using the multislice (**c**) and single-slice (**f**) phase retrieval methods. Panel (**c**) is the same as shown in Fig. 2d. The 3D Fourier transform of the multislice reconstruction (**c**) shows a maximum resolution of 1.6 Å, whereas that of the single-slice reconstruction (**f**) shows a maximum resolution of 2.0 Å.

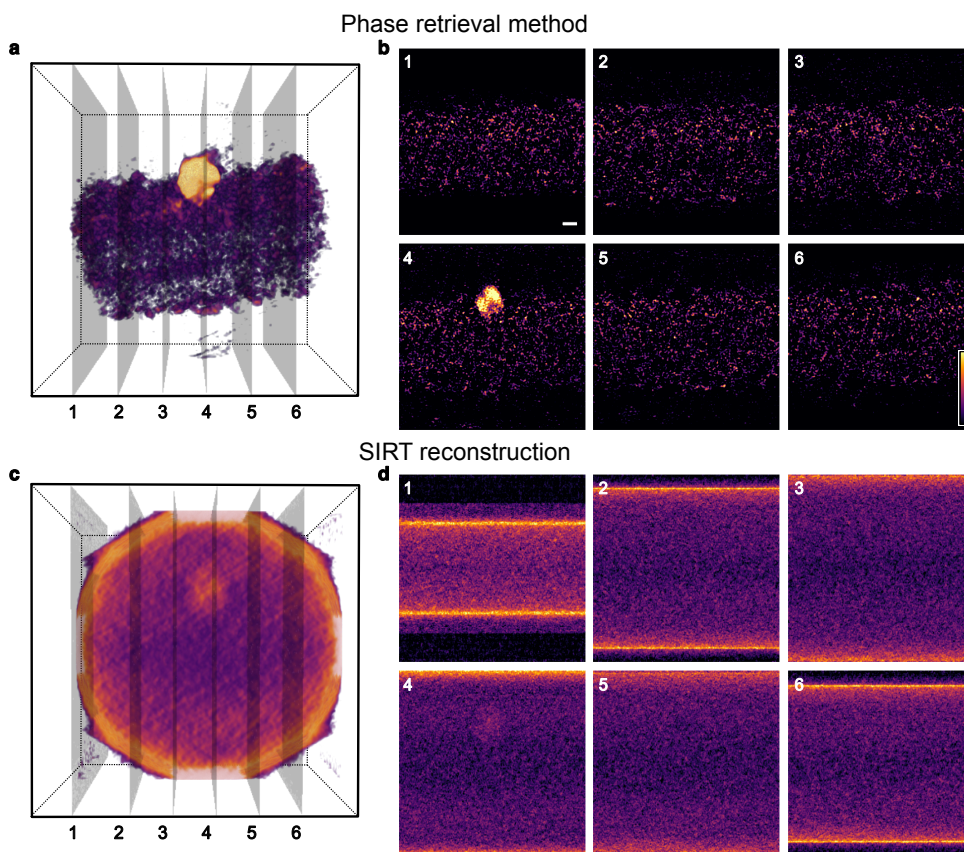


Fig. S3 Slices from Large-Area PhaseTEM Reconstructions for the Co_3O_4 nanoparticle. **a, c,** 3D density maps of the Co_3O_4 nanoparticle and the carbon support reconstructed using phase retrieval (a) and SIRT (c). The 3D volumes were reconstructed with a voxel size of 2.08 Å. **b, d,** 4 Å-thick slices extracted from the 3D reconstructions in (a) and (c), respectively. The numbers in (a) and (c) indicate the slice positions corresponding to the numbered slices shown here. Scale bar: 4 nm.

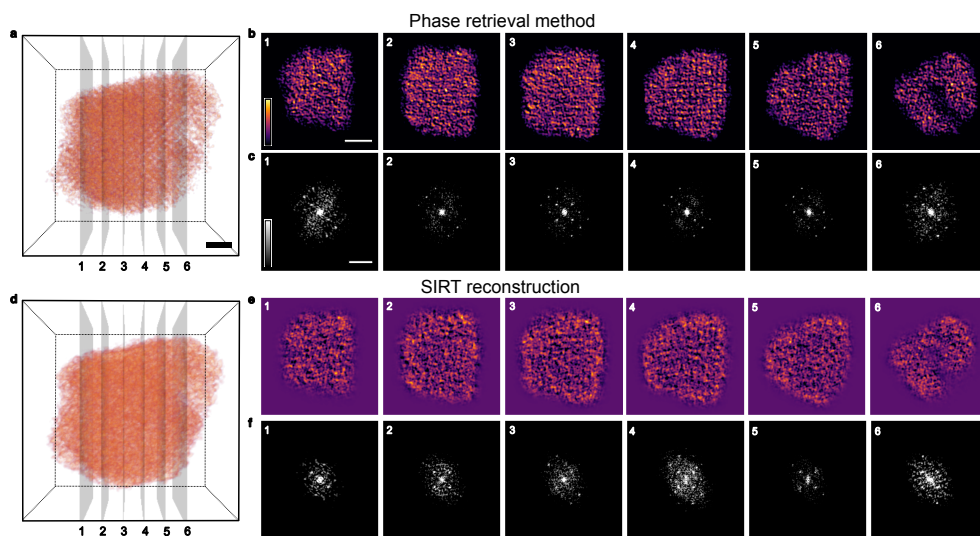


Fig. S4 Slices from Small-Area 3D PhaseTEM Reconstructions of the Co_3O_4 nanoparticle and Their 2D Fourier Transforms. **a, d,** 3D density maps of the Co_3O_4 nanoparticle reconstructed using phase retrieval (**a**) and SIRT (**d**), after applying a 3D mask to remove the carbon support intensity. The volumes were reconstructed with a voxel size of 0.52 Å. Scale bar: 1 nm. **b, e,** 1 Å-thick slices extracted from the 3D reconstructions shown in (**a**) and (**d**), respectively. The slice numbers in (**b**) and (**e**) correspond to the positions indicated in the 3D reconstructions in (**a**) and (**d**), respectively. Scale bar: 2 nm **c, f,** 2D Fourier transforms of the slices in (**b**) and (**e**), respectively. Scale bar: 0.4 Å⁻¹.

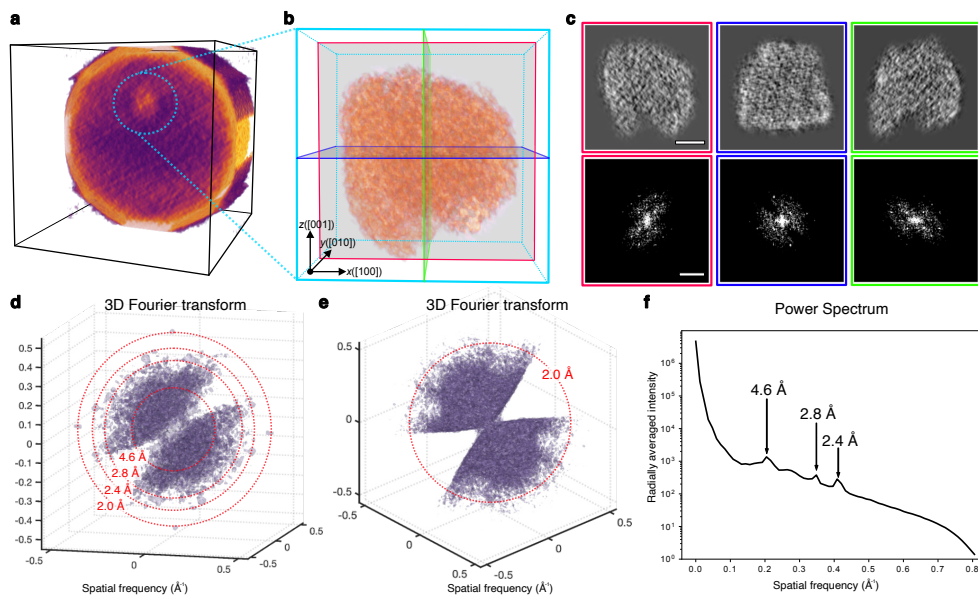


Fig. S5 Conventional SIRT Reconstruction and Resolution Analysis. **a**, Half-sectioned 3D density map illustrating the internal cross-section of the full 3D SIRT reconstruction of a Co_3O_4 nanoparticle embedded in a carbon support. **b**, 3D density map of the Co_3O_4 nanoparticle after applying a 3D mask to remove the carbon support. Scale bar: 1 nm. **c**, Top panel: 2-Å thick central slices of the 3D reconstruction in (b), with each color frame corresponding to the slice color in the 3D reconstruction. Bottom panel: 2D Fourier transform of the central slice shown in the top panel. Scale bars: Top panel, 2 nm; Bottom panel, 0.4 \AA^{-1} . **d**, 3D Fourier transform of the reconstruction in (b), displaying diffraction peaks at 2.0 Å resolution. **e**, 3D Fourier transform of the reconstruction in (b) from a different view, highlighting the missing wedge region. The image clearly shows no diffraction peaks within the missing wedge. **f**, Power spectrum of the 3D reconstruction in (b), indicating a resolution of 2.4 Å.

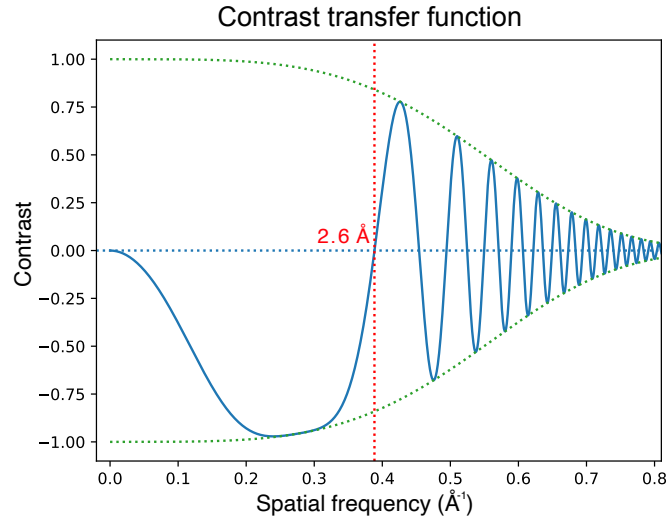


Fig. S6 Contrast transfer function (CTF) curve under the experimental conditions. The Scherzer defocus value was calculated using an optimized spherical aberration (C_3) value of 2.3 mm. The green dotted line represents the chromatic envelope function, computed using typical chromatic aberration (C_C) of 2.7 mm and an energy spread (ΔE) of 0.7 eV for the Titan Krios G3i microscope. The resulting contrast transfer function (CTF) indicates a diffraction-limited resolution of 2.6 Å.

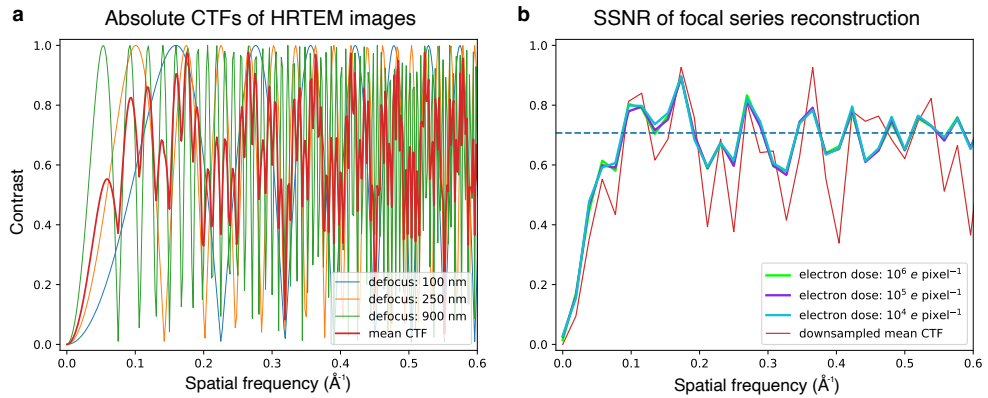


Fig. S7 Spectral Signal-to-Noise Ratio (SSNR) of 2D Focal Series Reconstruction. **a**, Simulated CTFs for defocus values of 100, 250, and 900 nm. **b**, SSNRs of focal series reconstructions using HRTEM images with defocus values of 100, 250, and 900 nm. For simplicity, the SSNRs of the focal series reconstruction are simulated under idealized conditions, assuming no chromatic aberration and using a single-slice reconstruction model.

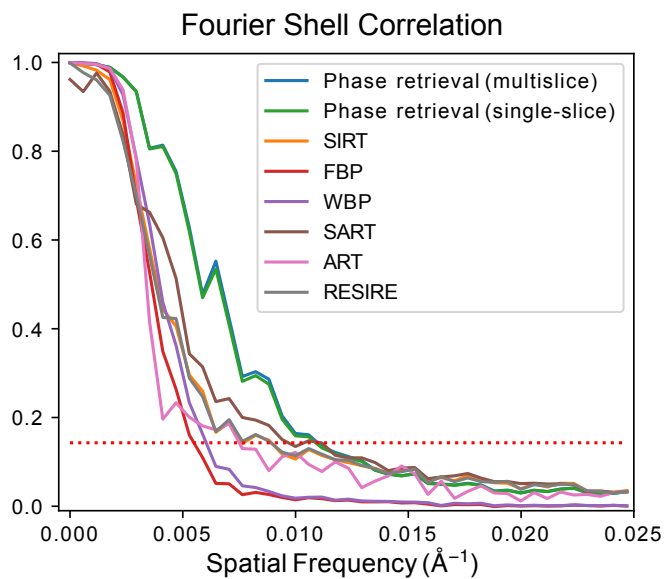


Fig. S8 Fourier shell correlation (FSC) from various reconstruction methods. FSC curves of HIV-1 particle reconstructions are compared across different methods: multislice phase retrieval (PhaseT Ξ M), single-slice phase retrieval (PhaseT Ξ M), simultaneous iterations reconstruction technique (SIRT), filtered back projection (FBP), weighted back projection (WBP), simultaneous algebraic reconstruction technique (SART), algebraic reconstruction technique (ART), and real space iterative reconstruction (RESIRE). The FSC resolutions, determined at the 0.143 criterion, are 9.0, 9.0, 13.1, 17.0, 15.5, 10.0, 13.1, and 10.6 nm, respectively.

Pseudo code for 3D reconstruction algorithm

Algorithm 1: Psuedo code to reconstruct 3D electrostatic potential

input : A tilt and focal series of measured HRTEM images $\{I_{\theta,\Delta f}\}$, Tilt angle set $\{\theta\}$, Defocus value set $\{\Delta f\}$, Step size of the gradient descent method α , Number of iterations: N_{iter}

output: 3D electrostatic potential $V(x, y, z)$

```

1  $V_{(1)}(x, y, z) \leftarrow 0$ 
   /* main reconstruction */
2  $\psi_0(x, y) \leftarrow 1$ 
3 incident parallel electron wave function
4  $P(q_x, q_y) \leftarrow$  free-space propagation with thickness  $\Delta z$  (Eq. ??)
5 for  $i$  in  $\{1$  to  $N_{\text{iter}}\}$  do
6   for  $\theta$  in tilt angle set  $\{\theta\}$  do
7      $V_{\text{rot}}(x, y, z) = R_{\theta}V_{(i)}(x, y, z)$ 
       /* forward propagation */
8      $\psi_1(x, y) \leftarrow \psi_0$  initial function
9      $V_m^{2D}(x, y) \leftarrow$  projected potential set from  $V_{\text{rot}}(x, y, z)$ 
10     $\{t_m(x, y)\} \leftarrow$  transmission function set from  $\{V_m^{2D}(x, y)\}$ 
11    for  $m$  in  $\{1$  to  $N_z\}$  do
12       $\psi_{m+1}(x, y) \leftarrow \mathcal{F}^{-1}[P(q_x, q_y)\mathcal{F}[t_m(x, y)\psi_m(x, y)]]$ 
13    end
14     $\psi_{\text{exit},\theta}(x, y) \leftarrow \psi_{N_z+1}(x, y)$ 
15    for  $\Delta f$  in  $\{\Delta f\}$  do
16       $\psi_{\text{final},\theta,\Delta f}(x, y) \leftarrow \mathcal{F}^{-1}[\psi_{\text{exit},\theta}(q_x, q_y) \exp(-i\chi(q_x, q_y))]$ 
17       $\hat{I}_{\theta,\Delta f}(x, y) \leftarrow |\mathcal{F}(\psi_{\text{final},\theta,\Delta f}(x, y))|^2$ 
18    end
       /* backpropagation */
19     $\psi_{N_z+1}^{\text{back}}(q_x, q_y) \leftarrow \sum_{\Delta f} \exp(i\chi(\Delta f)) \mathcal{F}(\psi_{\text{final},\theta,\Delta f} - \sqrt{I_{\theta,\Delta f}} \frac{\psi_{\text{final},\theta,\Delta f}}{|\psi_{\text{final},\theta,\Delta f}|})$ 
20    for  $m$  in  $\{N_z$  to  $1\}$  do
21       $\psi_m^{\text{back}}(x, y) \leftarrow \mathcal{F}^{-1}[P_m^*(q_x, q_y) \psi_{m+1}^{\text{back}}(q_x, q_y)]$ 
22       $\nabla_V \mathcal{E}^2(x, y, m) \leftarrow \text{Re}(-i t_m^*(x, y) \psi_m^*(x, y) \psi_m^{\text{back}}(x, y))$ 
23       $\psi_m^{\text{back}}(q_x, q_y) \leftarrow \mathcal{F}[t_m^*(x, y) \psi_m^{\text{back}}(x, y)]$ 
24    end
       /* update 3D potential */
25     $V_{\text{rot}}(x, y, z) \leftarrow V_{\text{rot}}(x, y, z) - \alpha_V \nabla_V \mathcal{E}^2(x, y, z)$ 
26     $V_{(i)}(x, y, z) \leftarrow R_{\theta}^{-1}V_{\text{rot}}(x, y, z)$ 
27  end
28 end
29  $V(x, y, z) \leftarrow V_{(N_{\text{iter}})}(x, y, z)$ 

```
